Rev. Roum. Sci. Techn.– Électrotechn. et Énerg.
Vol. **68**, *2*, pp247–250, Bucarest, 2023

DEVELOPMENT OF A NEW ONE-EYE IMPLANT BY 3D BIOPRINTING TECHNIQUE

TOPOR ALEXANDRU[1], ULIERU DUMITRU[2], RAVARIU CRISTIAN[1], BABARADA FLORIN[1]

Keywords: Eye implant; Digital imaging and communications in medicine (DICOM); Implant mounting.

The paper analyzes the possibility of implementing a new eye implant using the 3D bioprinting technique and the experimental model underlying it. The paper includes the stages of image processing using Digital Imaging and Communications in Medicine (DICOM) and the processing of the eye implant, results, and exploitation. In the exploitation part of the eye implant, the aims are optimizing the image processing stages and refining the precision of the calibration model. In the manufacturing part, the new eye implant is fabricated with the help of machines. These machines are suitable for manufacturing structures with their porosity controlled by additive manufacturing techniques. The feasibility of using 3D printing techniques using biocompatible materials in structures with predetermined porosity was demonstrated to manufacture a customized eye implant using medical imaging Computed Tomography (CT) results. The work was performed within the OrbImplant Project.

1. INTRODUCTION

New bioengineering products reduce medical risks in some rehabilitation processes [1] and help patients who use prostheses [2]. The manufacturing process of the new ocular implant uses a combination of modern technologies [3] for rapid prototyping/manufacturing [4], through 3D printing [5-7] additive processes, starting with computed tomography (CT) images collected techniques [8].

From tomographic images, image processing techniques will be applied to obtain the digital model that accurately describes the required shape of the custom implant [9]. The medical device gives monochrome images in a section. Image is a function of two-dimensional intensity f (x, y), where x and y represent spatial coordinates, and f is the brightness function that is proportional in each point (x, y) to the image's gray level at that point. A discretization is obtained both in spatial coordinates and in brightness. In terms of data structure, the image becomes a matrix at which the index of the row and that of the column respectively identify a point in the image, and the corresponding element of the matrix represents the gray level in that point. The elements of such a digital network are called image elements or pixels. The number of gray levels is chosen as the power of 2. A typical digital image size is 512 x 512 pixels, with 256 gray levels. The image's resolution is given by the total number of pixels per inch (PPI) and by the fidelity of the representations of the gray level (color depth). Image processing involves a succession of hard and soft processing steps and the implementation of theoretical methods. The goal is to find a solution to a given problem with the available means related to image processing. In the present application, the information is provided by computed tomography, and the objective is to achieve the selection and 3D reconstruction of each structure of interest (cavity, eyeball).

The first step in this process is the acquisition of images, which requires an image sensor as a CT scanner, with the ability to digitize the signal from its output. After obtaining the digital image, the next step is its preprocessing, *i.e.*, optimizing the image quality to increase the chances of success of further processing [10]. The next step is to segment the image, a concept that describes its "division" into constituent parts or distinct objects. Sophisticated segmentation algorithms require complicated calculations and a long processing time. Simple or insufficiently developed algorithms cannot be applied with high chances of success. Thus, a compromise solution must be chosen between the processing time and the results' quality. The result of the segmentation is usually a series of pixel intensities representing the contour of the region to be considered. The recognition and interpretation of the data are pursued in the last stage. Recognition is the process of classifying an object into a certain category based on information from the segmented image descriptions. These steps are followed in the current application. The data obtained by computed tomography will be subjected in the first phase to image processing algorithms to determine the contour of the cavity's individual sections at different sectioning levels. The representation of the cavity itself will be composed of a series of images that represent the contour of the sections through it. In the second phase, aggregate the series of images in a format compatible with 3D printing machines [11,12]. A diagram of the different methods of transforming the data obtained by computed tomography in initial graphics exchange specification (IGES) format is presented in Fig 1. The 3 methods presented involve different levels of complexity in implementation and result in different levels of fidelity for the model obtained:

1. Medical computer-aided design (MedCAD) Interface has low complexity, fast implementation, unsuitable for complex surfaces and low-quality results,
2. Reverse engineering has high complexity, long-lasting implementation, suitable for complex surfaces and high-quality results,
3. Standard tessellation language (STL) Interface has medium complexity, fast implementation, and may be unsuitable for certain complex surfaces and medium-quality results.

Depending on the complexity of the surfaces and their accuracy in the finished product, it is decided on the right data processing/preparation method. In the first phase, processing through the STL interface is selected for spherical surfaces. If the initial results are unsatisfactory,

[1] Faculty of Electronics Telecommunications & Information Technology, University Politehnica of Bucharest, Bucharest, Romania. E-mail: topor.alexandru@gmail.com; cristian.ravariu@upb.ro; florin.babarada@upb.ro
[2] SC Sitex 45 SRL, Bulevard Ghica Tei 114, Bucharest, Romania. E-mail: dumitru_ulieru@yahoo.com.hk

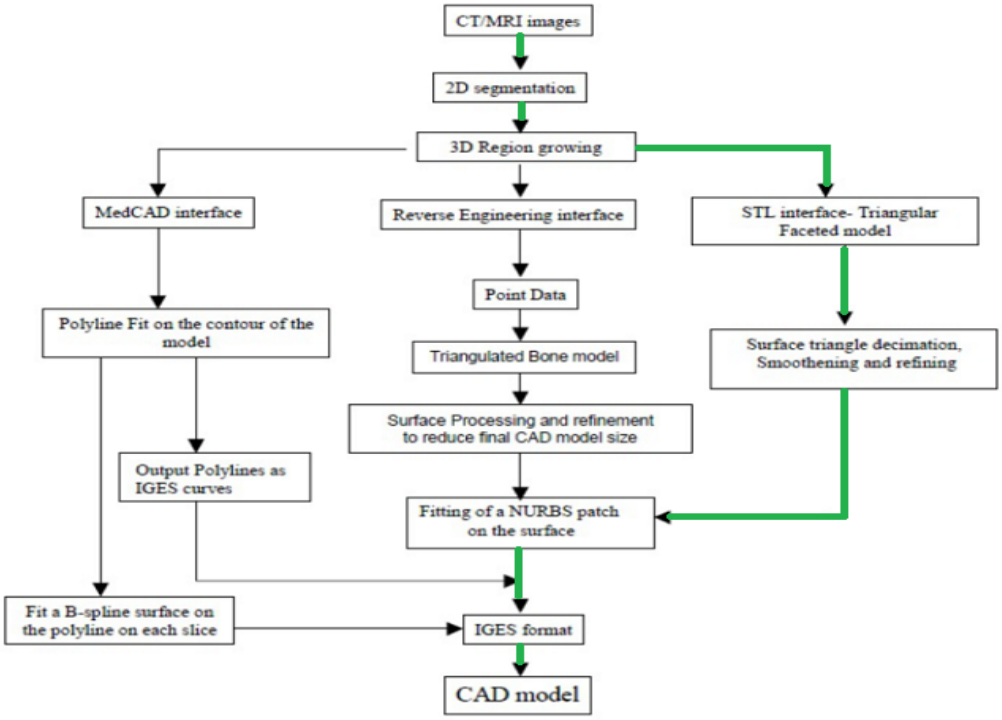

Fig. 1 – Methods of transformation from CT images into IGES format, the flow (marked in green) will be used for ocular reconstruction.

the Reverse Engineering method is applied during a second phase. The STL interface should represent a spherical pattern as accurately as possible by increasing the number of triangles used for mosaicking or tessellation [13].

2. DICOM IMAGE PROCESSING

To implement the steps described, a dedicated application was developed based on the DeVide software suite [14] developed by researchers at Delft University. To achieve the objective, selection, and 3D reconstruction of the eyeball, the application follows the following steps:

●**S1**. In the first phase, the data is loaded in digital imaging and communications in medicine (DICOM) format [15] using the DICOMReader block, the data being a collection of .dcm files that contain the information following the computed tomography (in this case, it is 460 of files, the information on the z-axis consisting of 460 samples, i.e. "slices"). The "Carol Davila" University of Medicine and Pharmacy delivered the images obtained from patients in the clinical study. To visualize the uploaded data, the slice3dVWR block is used.

●**S2**. This stage involves determining an area of interest and the range of pixel intensity values that characterize that area. The Hounsfield (HU) scale in medical imaging represents a quantitative measurement method for evaluating radiodensity, each substance in a certain range of HU values.

The Hounsfield scale is quantitative for describing radiodensity, commonly used in CT, MRI, or equivalent acquisition. Air has HU ~1000, lung ~700, soft tissue ~300÷~400, fat ~84, water 0, cerebrospinal fluid 15, blood +30÷+45, muscle tissue +40, bone +700 for spongy bones to +3000 for dense bones [16].

These values are the basis for defining the response range of different organs according to their chemical composition. This consistency allows the application of a double Threshold block in the DeVide application that will select only the intensity zones in a certain range of values. A trial-and-error process will determine the minimum and maximum values optimal for selecting the area of interest and is set in the doubleThreshold block. These values in the case of the eyeball are 0.00 and 20.00 (extraction of aqueous humor), the resulting visualization module presented in Fig. 2.

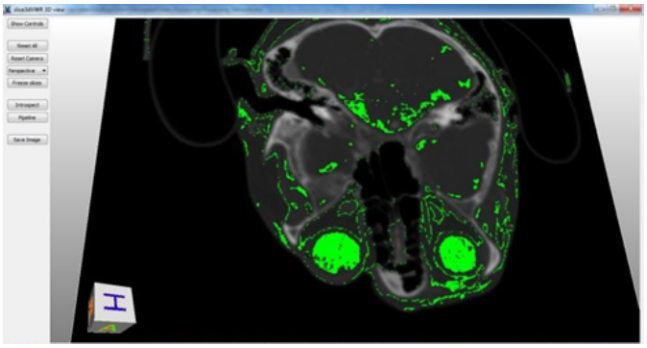

Fig. 2 – DiVide network with double Threshold block. Selected regions (green) that fall within the set value range 0-20.

●**S3**. This stage involves defining a seed point on the eyeball, around which the desired contour will be built, the seed point being the yellow one in Fig. 3. With the help of the defined point, the seedConnect block is used, which will reunite the points connected to the seed point which are also in the range defined by double Threshold. Closing and contour blocks are connected to the output of the seedConnect block. The resulting network and the visualization module are presented in Fig. 4. The successful eyeball extraction can be observed, resulting in the red body.

●**S4**. The next step involves applying the wsMeshSmooth block, which aims to unify some outer polygons to achieve a smoother contour. The QuickInfo block provides information about the resulting body, consisting, in this case, of 13648 polygons. It can optionally be applied to a vtkQuadricDecimation block that can reduce the number of polygons by an interpolation algorithm.

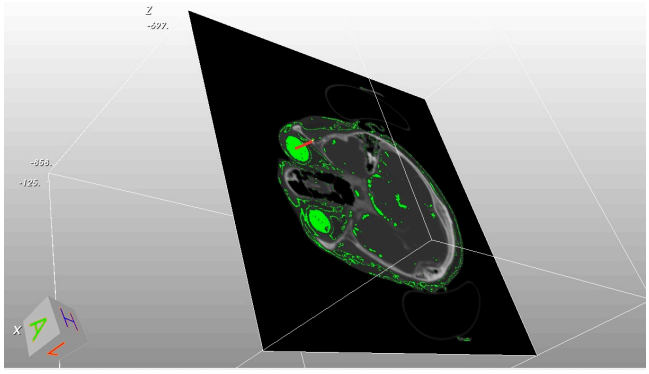

Fig. 3 – Selecting the seed point (red) around which the desired region will be built.

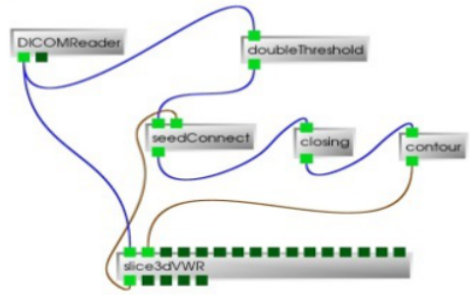

Fig. 4 – The resulting network (up) and the body are automatically reconstructed by the closing and contour blocks (down).

Finally, the stlWRT block connected to the QuadricDecimation output will export the result in STL format. The final network is presented in Fig. 5. and the result in Fig. 6.

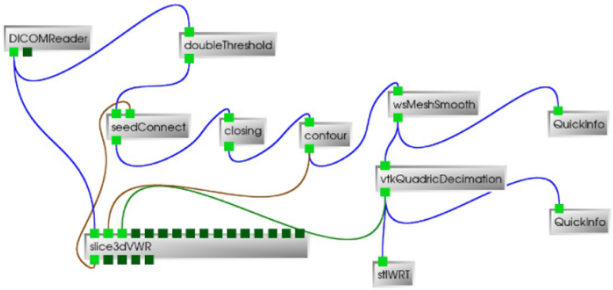

Fig.5 – DeVide network for the realization of the processing algorithm that extracts the discretized model (.stl).

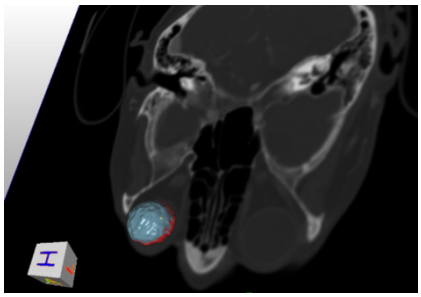

Fig. 6 – The discretized model (.stl) of the region of interest, the eyeball.

●**S5**. For post-processing, the exported.stl file is loaded into the MeshLab software (Fig. 7 left) where additional processing procedures can be applied to finish the surface and reduce edge effects, as presented in Fig. 7 (right).

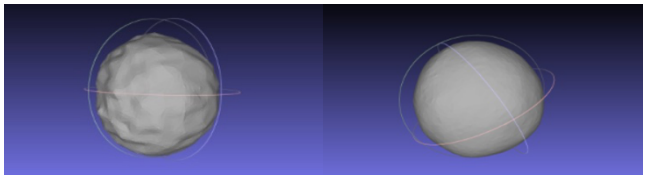

Fig. 7 – (left) The .stl file exported from DeVide and uploaded to MeshLab. (right) Final .stl model for rapid prototyping by additive manufacturing.

3. REALIZATION OF THE EYE IMPLANT

Eye implant realization starts from several medical imaging devices. It continues with fine-tuning necessary to adjust the differences in image quality and pixel intensity range in the region of interest. The reconstruction parameters start from the assumption that different medical imaging devices will give the answer in the same range on the Hounsfield scale for the same areas of interest, and fine-tuning step is necessary to cover the variations [17]. These results must have the aesthetics for facial prosthetic implants [18]. For the manufacturing stage, the model of the ocular implant can be used in machines to manufacture structures with controlled porosity through additive manufacturing techniques [19, 20]. Porous structures are superior to the corresponding compact parts [21, 22].

Lattice microstructures offer huge potential for their use in the design of cellular structures with low specific weights. The attention was focused on the relationship between microstructure-mechanical properties-deformation. This relationship allows the optimization of the structure design depending on the mechanical loads to which it is subjected. The final goal is to obtain customized implants with mechanical characteristics like those of the organ to replace. Selective Laser Melting (SLM) technology is considered a real and viable alternative in achieving precise control over the architecture of the scaffold-shaped structure, over the shape of the pores, but more so of the interconnectivity, which is crucial for tissue growth. Porosity is the total percentage of empty spaces in a solid and is a material-independent morphological property. Newly developed architectures offer superior rigidity and strength relative to the structure's mass compared to those offered by metal foams.

One such example is the architecture and machinability of cellular structures based on a special type of elementary cell called the "Schon" thyroid [23], which has a special feature: smooth cylindrical bars converge uniformly to a spherical nucleus. The angle of inclination of the cylindrical bars of the thyroid varies continuously towards the spherical core. This feature offers the possibility that during the SLM process, the previously fabricated layer supports the next layer so that such a structure is self-supporting without additional interior support structures. Figure 8 shows this special structure at different levels of porosity. To achieve this, a thyroid structure was used, which kept a constant ratio of 15 % between the volume occupied by the bars and the core at different sizes of the elementary cell: 2, 3.5, 4.5, 5, 6.5, and 8 mm [22].

Finally, the problem that must be solved to make it possible to achieve structures with geometrically defined porosity is to find the shape of the elementary cell.

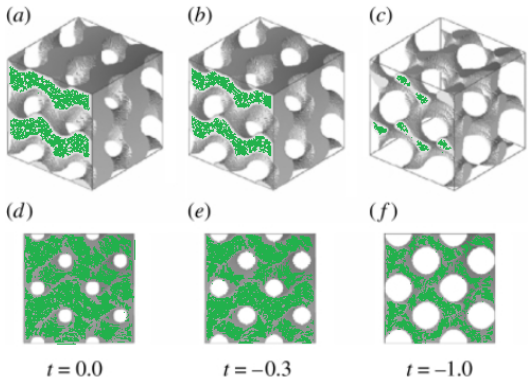

Fig. 8 – Structures with different degrees of porosity, based on the thyroid "Schon." The t value refers to the wall thickness degree of the honeycomb structure: a) 3D view at t=0, d) 2D view at t=0; b) 3D view at t= -0.3, e) 2D view at t= -0.3; c) 3D view at t=-1.0, f) 2D view at t= -1.0

These principles are the basis for obtaining geometric porosity, essential in the present application, to give the ocular implant the possibility of tissue proliferation within the structure, increasing, together with the carefully chosen types of material, the degree of biocompatibility of the implant. To manufacture the porous structures for the ocular implant, the starting steps are the results of modeling and simulation of 3D reconstruction by software/image processing methods.

4. CONCLUSIONS

The printing result is the implant itself, shown in Fig. 9. The eye implant was obtained from the cranial CT scans. The image processing algorithms were applied to extract the .stl type model, obtaining a personalized digital representation of the cavity. The bioscaffold printing machine has been optimally configured to obtain the necessary structure and physicochemical characteristics. The implant thus obtained reaching the established objectives. The complete process of sample collection, image scanning, implant fabrication, mounting, and postoperative patient follow-up can be implemented in a pilot program.

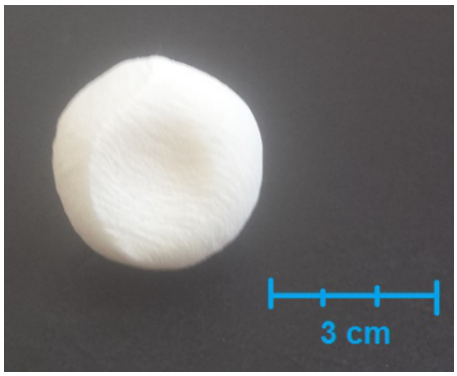

Fig. 9 – Experimental model of the eye implant.

The feasibility of using 3D printing techniques using biocompatible materials in structures with predetermined porosity to manufacture a custom eye implant using medical imaging (CT) results has been demonstrated. The results were published [23], and for these results, a patent was granted to the contributors to the project [24]. The modernity and innovation brought by this technique were awarded a silver medal at the International Exhibition of Inventions in Geneva in 2019.

REFERENCES

1. V. Potop, V. Coviltir, C. Corbu, M. Burcel, C. Ionescu, D. Dascalescu, *Corneal hysteresis, a glaucoma risk factor independent of the intraocular pressure*, Rev. Roum. Sci. Techn.– Électrotechn. Et Énerg., **64**, *3*, pp. 297–300 (2019).
2. I. Stanica, F. Moldoveanu, M. Dascalu, A. Moldoveanu, G.-P. Portelli, C. Bodea, *Neurorehabilitation system using virtual reality and myo armband for patients and medical personnel training*, Rev. Roum. Sci. Techn.– Électrotechn. Et Énerg., **65**, *1-2*, pp. 139–144 (2020).
3. N. Bentabet, N. Berrached, *An efficient asynchronous brain-computer interface for assistive technology: a novel approach,* Rev. Roum. Sci. Techn.– Électrotechn. Et Énerg., **65**, *1-2*, pp. 131–137 (2020).
4. O. Abdulhameed, A. Al-Ahmari, W. Ameen, *Additive manufacturing: challenges, trends and applications*, Advances in Mechanical Engineering, **11**, *2*, pp. 1-27 (2019).
5. T. Raynaa, L. Striukovab, *From rapid prototyping to home fabrication: how 3D printing is changing business model innovation*, Technological Forecasting and Social Change, **102**, pp. 214-224 (January 2016).
6. E. Koçak et al., *Three dimensional bioprinting technology: applications in pharmaceutical and biomedical area*, Colloids and Surfaces B: Biointerfaces, **197** (2021).
7. A.C. Sommer et al., *Implementations of 3D printing in ophthalmology*, Graefe's Archive for Clinical and Experimental Ophthalmology, **257**, pp. 1815–1822 (2019).
8. M.J. Willemink, P.B. Noël, *The evolution of image reconstruction for CT – from filtered back projection to artificial intelligence*, Eur. Radiol., **29**, *5*, pp. 2185–2195 (2019).
9. A. Pugalendhi et al., *Design and development of model eye for retina laser by using additive manufacturing*, Proc. of the Institution of Mechanical Engineers, Part H: Journal of Engineering in Medicine, **235**, *1*, pp. 89-98 (2021).
10. M. Curilă, S. Curilă, C. Grava, *Geometry compression for 3D models*, Rev. Roum. Sci. Techn.– Électrotechn. et Énerg., **61**, *2*, pp. 201–204 (2016).
11. R.D. Larochelle et al., *3D Printing in eye care*, Ophthalmol. Ther., **10**, *4*, pp. 733-752 (2021).
12. T.M. Shiju et al., *3D in vitro corneal models: a review of current technologies*, Experimental Eye Research, **200** (2020).
13. W. Zeng, X. Jiang, P. J. Scott, T. Li, *A new method to characterize the structured tessellation surface*, Procedia CIRP, **10**, pp. 155–161 (2013).
14. M. Eibl, *DEViD: A media design and software Ergonomics integrating visualization for document retrieval*, Information Visualization, **1**, *2*, pp. 139-157 (2022).
15. M.D. Herrmann et al., *Implementing the DICOM standard for digital pathology*, Journal of Pathology Information, **9**, *37*, pp. 1-16 (2018).
16. A.O. Hebb, A.V. Poliakov, *Imaging of deep brain stimulation leads using extended Hounsfield Unit CT*, Stereotactic and Functional Neurosurgery, **87**, *3*, pp. 155-160 (2009).
17. R. Cadle et al., *An image analysis-based workflow for 3D bioprinting of anatomically realistic retinal vascular patterns*, Bioprinting, **23** (2021).
18. J. Klimczak, S. Helman, S. Kadakia, R. Sawhney, M. Abraham, A. K. Vest, Y. Ducic, *Prosthetics in facial reconstruction*, Craniomaxillofac. Trauma Reconstr., **11**, *1*, pp. 6–14 (2018).
19. Y. Bozkurt et al., *3D printing technology; methods, biomedical applications, future opportunities and trends*, Journal of Materials Research and Technology, **1**, *4*, pp. 1430-1450 (2021).
20. A.J. Sheoran et al., *Bio-medical applications of additive manufacturing: a review*, Procedia Manufacturing, **51**, *7*, pp. 663-670 (2020).
21. L. Hodásová et al., *Polymer infiltrated ceramic networks with biocompatible adhesive and 3D-printed highly porous scaffolds*, Additive Manufacturing, **39** (March 2021).
22. S. Iyer, M. Alkhader, T.A. Venkatesh, *Electromechanical response of piezoelectric honeycomb foam structures*, Journal of the American Ceramic Society (2013).
23. D. Ulieru, A. Topor, X. Vila, O.M. Ulieru, *Great flexibility nanomanufacturing technology concept of new ocular implant with high biocompatibility degree and fast proliferation speed*, EuroNanoForum Conference, La Valletta, Malta, pp. 21-23 (2017).
24. L.M. Popescu, R.M. Piticescu, A.M. Motoc, L.M. Voinea, S.L. Grădinaru, D. Ulieru, A. Topor, *Three-dimensional structures based on hydroxyapatite and polyurethane-diol, obtained by the 3D printing technique*, Invention Patent No. 132753 issued by OSIM.